

Radionuclide Containment Properties of Fractured and Faulted Volcanic Tuff Units at the T-Tunnel Complex, Rainier Mesa, Nevada National Security Site – 14013

Donald M. Reeves¹, Rishi Parashar¹, Karl Pohlmann², Eric M. LaBolle³, Yong Zhang², Chuck Russell², and Jenny Chapman²

¹ Division of Hydrologic Sciences, Desert Research Institute, 2215 Raggio Parkway, Reno, NV 89512.

² Division of Hydrologic Sciences, Desert Research Institute, 755 E. Flamingo Rd, Las Vegas, NV, 89119.

³ Department of Land, Air and Water Resources, University of California, 137 Veihmeyer Hall, Davis, CA, 95616.

ABSTRACT

Rainier Mesa, a tuffaceous plateau on the Nevada National Security Site, has been the location of numerous subsurface nuclear tests conducted in a series of tunnel complexes constructed approximately 400 m below the top of the mesa and 400 m above the regional groundwater flow system. The tunnels were constructed near the middle of an 800 m thick Tertiary volcanic sequence of faulted, low-permeability welded and non-welded bedded, vitric, and zeolitized tuff units. This multi-year study evaluates the potential at the T-tunnel complex for downward radionuclide transport to the regional water table over a 1,000 year regulatory time period. A dual-permeability NUFT flow model containing spatially discontinuous, poorly-connected fault networks within low-permeability, porous tuff units is utilized to simulate complex patterns of variably-saturated flow. RWHet, a fully Lagrangian, random-walk particle tracking code, was modified for this project to simulate advective-dispersive particle motion in dual-permeability flow fields with diffusional mass exchange between fractures and matrix. Flow and transport simulations were executed in a Monte Carlo framework that incorporated a source term of ten radionuclides for six underground tests and parametric uncertainty in transport parameters. Ensemble breakthroughs at the water table of conservative radionuclides over the 1,000 year regulatory time period are extremely small and do not exceed regulatory limits for the estimated range of recharge flux. A comprehensive analysis of the T-tunnel site and resultant numerical model is performed to identify properties of the tuff units that promote containment of radionuclides within the Tertiary volcanic sequence. Features important for the limited breakthrough include the conceptual model of fluid flow through the perched groundwater flow system, recharge estimates, hydraulic and geochemical properties of the geologic units, diffusional mass transfer between fractures and matrix blocks, and configurations of the fault and fracture networks.

INTRODUCTION

Rainier Mesa is a high elevation plateau located in the north-central portion of the Nevada National Security Site (NNSS) that hosted 61 underground nuclear tests in 13 tunnel complexes (Fig. 1). The focus of this study is on the T-tunnel complex, the site of six underground nuclear tests conducted between 1970 and 1987. The tunnel complex has an elevation of 1,707 m, extends 1.57 km to the west of a single portal, and has a north-south distance of 0.8 km [13]. The T-tunnel complex consists of over 10,600 m of tunnels mined within Tertiary-age volcanic rocks of the Tunnel Bed 2 through 4 members of the Tunnel

Formation (Ton2, Tn3, Tn4) and the Tub Spring Tuff (Tub) (Fig. 2). These geologic units are mostly comprised of ash-fall tuffs with zeolitic alteration, although a thin, welded, ash-flow subunit of the Tub Springs Tuff (Tub) is present. All tests were conducted in the Tn4, Tn3 and Ton2 Tunnel bed members at elevations of 1712 to 1717 m amsl and overburden thicknesses of 348 to 424 m [15]. The Lower Carbonate Aquifer 3 (LCA3), a laterally extensive carbonate aquifer system of Paleozoic age subjected to thrust faulting, underlies the Tertiary volcanics (Fig. 2).



Fig. 1. Detailed map of Rainier Mesa with the T-tunnel complex located slightly northeast of center. Small dots at the end of each tunnel complex denote an underground nuclear test. Large dots denote the locations of wells ER-12-3 and ER-12-4. The map encompasses an area of approximately 135 km². From [12].

Rainier Mesa receives a mean annual precipitation of 350 mm/yr. Estimated recharge rates for the T-tunnel complex region are variable and range from 11.5 to 15.2 mm/yr (3-4% mean annual precipitation) based on distributed-parameter INFIL3 models calibrated to 36-Cl concentrations in the T-tunnel waters [5]. Wells and piezometers drilled in the vicinity of the T-tunnel complex indicate the presence of a laterally extensive perched zone of saturation in the Tertiary volcanic rocks. This saturated zone has a hummocky upper surface with an elevation of approximately 1815 m at the T-tunnel complex. The precise vertical extent of saturation for this perched zone is unknown; however, inspection of water levels in wells and piezometers near the T-tunnel indicate that the vertical extent of saturation spans from the upper zone of pervasive zeolitization located in the Tn4 down to at least Ton1 [2,17]. This comprises most of the volcanic sequence underlying the T-tunnel complex (Fig. 2). A regional ground water flow system occurs in the LCA3 with a potentiometric surface at an elevation of 1315 m in the vicinity of the T-tunnel complex. An unsaturated zone was found to be present in the top 50 m of the LCA3 during drilling of ER-12-3 and ER-12-4 (refer Fig. 1 for locations of ER-12-3 and ER-12-4). In summary, water levels indicate that the T-tunnel complex is located approximately 100 m below the top of an upper zone of perched saturation and approximately 400 m above a regional ground water flow system located in the LCA3. These two saturated zones are separated by an unsaturated zone in the upper portion of the LCA3.

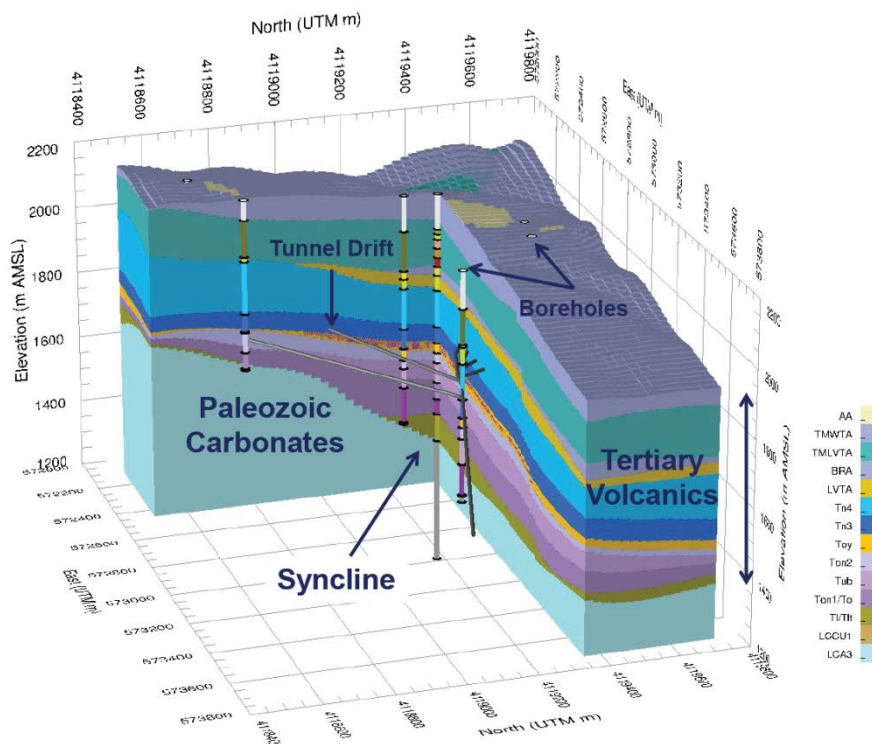


Fig. 2. Stratigraphic-hydrostratigraphic model of the T-tunnel complex region distinguishing between the Tertiary volcanics and underlying Paleozoic carbonates of the LCA3. A subset of boreholes used to develop this model are included. The tunnel complex is located at an elevation of 1715 m. Note the northeast trending synclinal structure. From [12].

The tunnel complex is oriented roughly perpendicular to multiple, approximately north-south trending normal faults with displacements up to 45 m (Fig. 3). Observed inflows into the tunnel complex from the perched zone of saturation were spatially discontinuous during tunnel operation and typically exhibited low discharge rates, although significant volumes of water up to $2.5 \times 10^{-2} \text{ m}^3/\text{s}$ (400 gpm) were encountered at two locations. The duration of the high inflow rates was short. Inflows occur along both the largest faults and smaller background fractures. Here we denote background fractures to be smaller-scale rock discontinuities without an appreciable amount of shear displacement, and are either joints or perhaps smaller faults where shear displacement is difficult to detect. The tunnel complex is angled slightly downward towards the portal to facilitate water drainage, with measured portal discharge values ranging from $1.0 \times 10^{-3} \text{ m}^3/\text{s}$ to $2.5 \times 10^{-2} \text{ m}^3/\text{s}$ over the history of the tunnel complex prior to portal sealing. These portal discharge trends were used as a novel transient calibration metric for the dual-permeability flow model of the T-tunnel complex [12].

The focus of this paper is on final radionuclide transport predictions from the T-tunnel complex generated from a series of calibrated, dual-permeability flow and transport models that simulate fluid flow and radionuclide migration through a series of variably-saturated, sparsely fractured and faulted Tertiary tuff units to a regional flow system in the underlying LCA3. Radionuclide source terms for the six underground tests, including source term and parametric uncertainty, are incorporated into a Lagrangian framework that simulates advective-dispersive particle motion in the dual-permeability flow fields and

diffusional mass exchange between fractures and matrix. Ensemble breakthroughs from the T-tunnel complex to the underlying water table over the 1,000 year regulatory time period are analyzed to understand how these transport results are linked to the complex hydrogeologic conditions at the site and fracture and fault properties of the Tertiary volcanic tuff units and the LCA3.

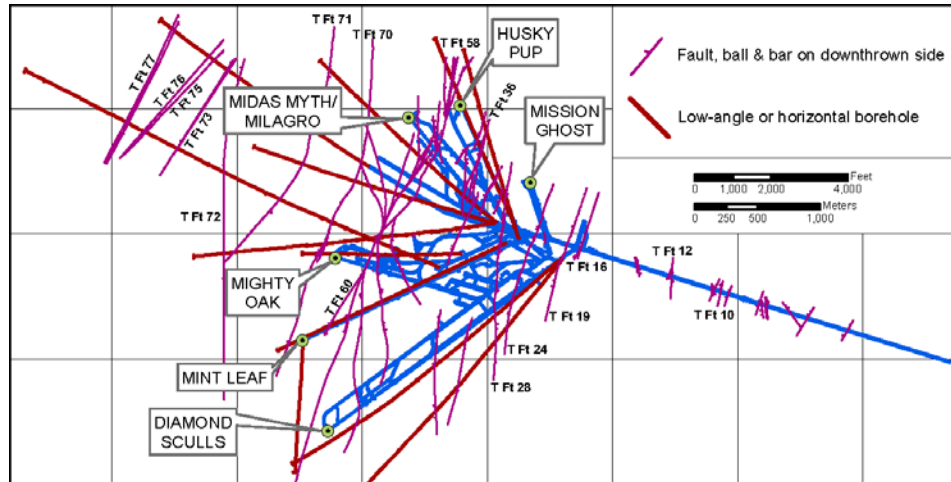


Fig. 3. T-tunnel complex showing tunnel drifts, intersected faults, and working points (green circles at end of drifts) with test names. All faults in this figure are included in the numerical model as deterministic features assigned to the fracture continuum nodes. From [12].

DUAL-PERMEABILITY FLOW SIMULATION AND CALIBRATION

The development of a robust conceptual model of flow and radionuclide transport was critical for both the development and parameterization of the T-tunnel complex dual-permeability model. This involved a comprehensive analysis of available geological, hydrological and geochemical datasets as detailed in [12]. The conceptual model is summarized in bulleted form below:

- A laterally and vertically extensive, perched zone of saturation is present within the zeolitized tuff units from Tn4 down to at least Ton1.
- Matrix permeability values of the tuff units below the T-tunnel complex are low enough to sustain observed perching under modern recharge fluxes.
- The dominant flow scenario involves downward flow of infiltrated precipitation through the low-permeability matrix and open fractures and faults of the Tertiary volcanic sequence to the underlying LCA3.
- Fault and fracture networks in the Tertiary volcanics are poorly-connected and span relatively small volumes of the rock mass.
- The T-tunnel complex may function as a macropore that provides hydrologic connection for fluid flow and radionuclide migration between otherwise unconnected, transmissive faults.

The T-tunnel complex numerical model was developed using the dual-permeability option of the NUFT USIP module to simulate variably-saturated flow in both fractures and matrix [6]. The north, south, and west model boundaries are 100 m from the nearest nuclear test, and the east model boundary occurs at the main drift where the tunnel complex is sealed (Fig. 4). The vertical extent of the model ranges from the top of the perched zone of saturation at 1815 m amsl to the water table in the LCA3 at 1315 m amsl. A

spatially variable recharge flux condition based on simulated net infiltration is applied to the top model boundary. Three recharge maps best calibrated to 36-Cl concentrations from the T-tunnel complex, R7 (11.5 mm/yr), R11 (15.2 mm/yr), and R29 (14.2 mm/yr), were used to represent low, high, and intermediate recharge flux scenarios, respectively [5]. No flow boundaries are assigned to the sides of the model and a water table boundary is assigned to the bottom of the model. Cell discretization in the model was influenced by the properties of the fault networks, in particular fracture density. A grid block size of 20m on a side was found to provide sufficient resolution of the mapped fault networks on the continuum grid.

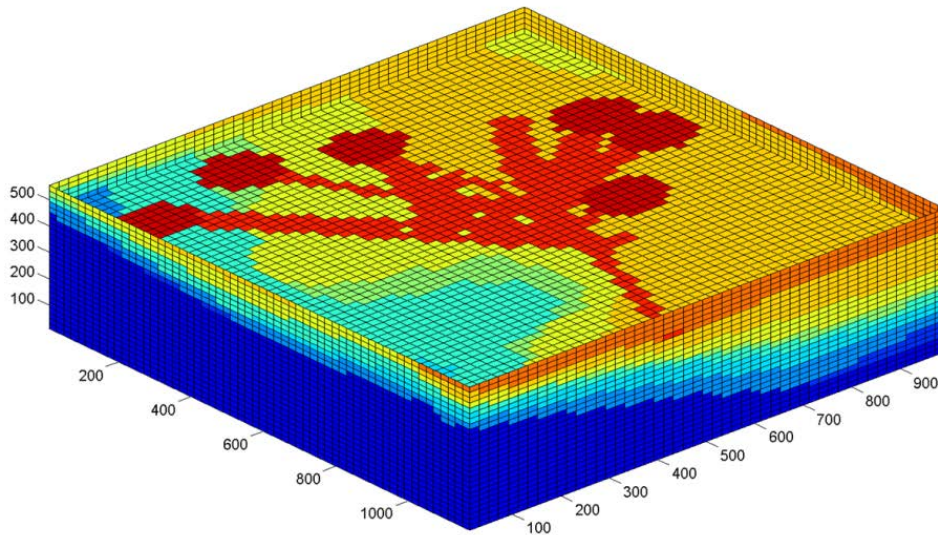


Fig. 4. T-tunnel complex model domain with cutout showing mapped tunnel horizon along with damage zones (circular features at the end of tunnel drifts). Flow barriers within the tunnel complex are also included in the model (not shown). All stratigraphic units shown as individual colors are zeolitic Tertiary volcanic tuffs, except for Paleozoic carbonates of the LCA3 which is denoted by the dark blue color. From [12].

Hydraulic properties including permeability, porosity, and unsaturated parameters were obtained from rock cores from the Tertiary volcanics and LCA3. These values are applied to the matrix continuum. A fracture continuum method, originally proposed by [9] and further refined by [8,12], is used to map fault networks generated according to site-specific fracture attributes onto a continuum grid. The fracture continuum approach preserves heterogeneity and flow anisotropy of fault networks through a series of fracture mapping rules as presented in [8,12].

Characterization of the fault data collected in the Tertiary tuff units along the tunnel drifts is consistent with the methods found in [10] where probability distributions are used to describe fault orientation, spacing, and length. The fracture analysis yielded one approximately north-south fault set with considerable scatter about the mean orientation. High degrees of spatial clustering were observed with an average spacing of approximately 12 m. The spatial clustering necessitated the development of a multiplicative cascade process conditioned on the largest faults mapped in Fig. 3. Discrete fracture network analyses determined that fracture clustering is essential in forming poorly-connected fault networks consistent with observations of flow and drainage from the tunnel complex (Fig. 5).

Representative networks for the Tertiary volcanics and Paleozoic carbonates of the LCA3 are shown in Fig. 6.

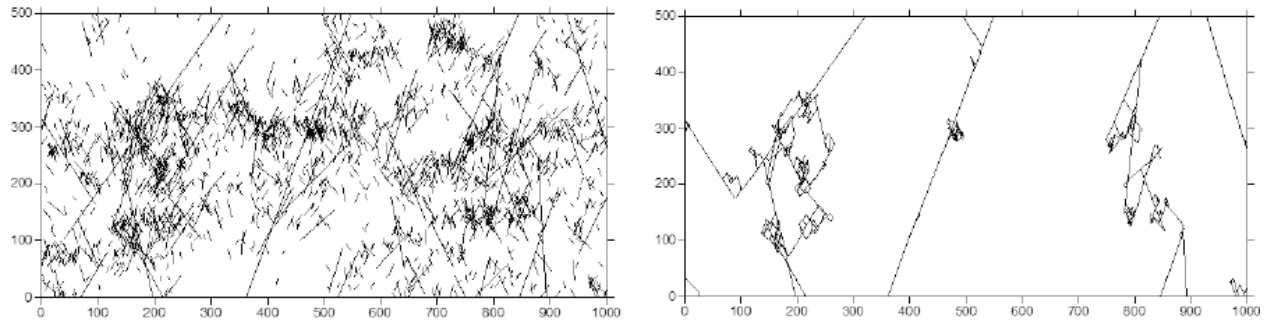


Fig. 5. Site representative discrete fracture network (left) along with isolation of hydraulic backbone (right) showing tree-shaped, poorly-connected fault networks. Distances are in meters. From [11].

The hydrogeologic complexity of the T-tunnel complex necessitated a multi-stage calibration effort to capture dominant flow characteristics of the site [11,12]. The model was first calibrated in steady-state using fault aperture to match the observed laterally and vertically perched water levels in the Tertiary volcanics with an upper elevation of approximately 1815 m, fracture saturations ranging from fully saturated to dry, and maintaining unsaturated conditions in the Paleozoic carbonates above the regional water table at 1315 m. A model with enhanced tunnel features was used to calibrate to the 24.1 year transient period of portal discharge. Details on the dual-permeability model development, parameterization and calibration can be found in [11,12]. A total of 20 flow realizations were generated for each of the R7, R11 and R29 recharge flux scenarios. All parameters in these realizations are constant, with the exception of the spatial configuration of the randomly-generated background faults.

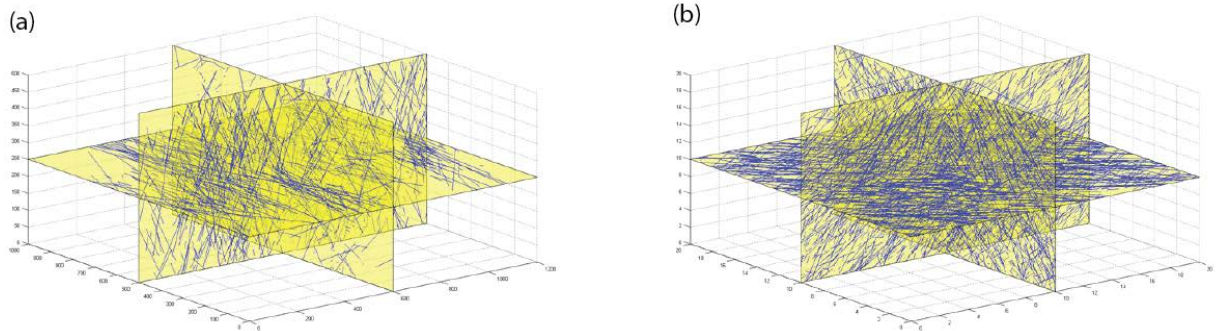


Fig. 6. Representative 3D fracture networks for (a) Tertiary volcanics and (b) Paleozoic carbonates projected onto three orthogonal planes for enhanced viewing. Note the strong contrast in density: the volcanic DFN is plotted onto a domain of 1 km by 1 km by 0.5 km, whereas the carbonate DFN is plotted onto a domain of 20 m by 20 m by 20 m (grid size used in the dual-permeability model). From [12].

RADIONUCLIDE TRANSPORT

A ten radionuclide source term is simulated for each steady-state flow realization. This source term is divided into a total of seven transport classes. Parametric uncertainty in the transport simulations is a function of variability in the tortuosity factor used to compute effective diffusion coefficients, sorption

coefficients used in the computation of matrix and fracture retardation, and glass dissolution. Uncertainty is also applied to the mass of each radionuclide in the source term and the size of the exchange volume over which the radionuclide particles are distributed. A total of 50 transport realizations are generated for each of the flow field realizations to fully explore the source term and parametric uncertainty.

Source Term and Radionuclide Mass

The radionuclide source term was developed by Lawrence Livermore National Laboratory (LLNL) scientists and includes: 3-H, 36-Cl, 90-Sr, 99-Tc, 129-I, 238-U, 238-,239-, 240-Pu and 241-Am. Each of these radionuclides was grouped into one of seven transport classes based on similarities in glass and hydraulic release fractions, free water diffusion coefficients, linear adsorption coefficients, and exchange volume size (Table 1). The glass and hydraulic release fractions, linear sorption (K_d) values, and exchange volume distribution as a function of cavity radius, $f(R_c)$, were extracted from data compiled by LLNL. Free water diffusion coefficients D^* were obtained from Underground Test Area (UGTA) transport parameter documents [14,16].

Table 1. Transport classes assigned to radionuclide source term. Note that the exchange volume multiplier (EV) is given as a function of cavity radius R_c . Plutonium isotopes contain two K_d values: the first is used to compute fracture retardation, while the latter is used to compute matrix retardation.

Class	Radionuclide	Glass	Hydraulic	D^* m ² /s	K_d log ₁₀ (ml/g)	σ_{Kd} log ₁₀ (ml/g)	EV
		%	%				f(R_c)
I	3-H	0	100	2.40E-09	0	0	1.5-3.0
II	36-Cl, 129-I	50	50	2.04E-09	0	0	1.5-3.0
III	99-Tc	80	20	2.04E-09	0	0	1.5-3.0
IV	90-Sr	40	60	1.29E-09	3.2	0.37	1.5-3.0
V	238-U	90	10	1.00E-09	0.34	0.29	1.0-1.5
VI	238-,239-,240-Pu	95	5	1.00E-10	0.53/2.53	0.37	1.0-1.5
VII	241-Am	95	5	3.06E-10	3.36	0.29	1.0-1.5

The initial mass at t_0 for radionuclides associated with each test is incorporated into the model through a series of steps. A total of 25,000 particles were uniformly distributed over the flooded tunnel complex and 12,500 particles were distributed over each of six exchange volumes (Fig. 7). The number of particles reflects a balance between the resolution of the radionuclide transport results and computational burden. Each particle is given a specific numeric identifier that allows for the identification of the source of particles that reach the water table within the 1,000 year regulatory compliance time frame. The mass of each breakthrough particle is then determined during post-processing. All particles are initially placed into the fracture continuum for conservatism.

The mass of each radionuclide associated with individual tests is decay-adjusted to a t_0 of 1992, corresponding to tunnel closure and the cessation of lateral diversion of flow and radionuclides out of the portal and into the T-tunnel containment ponds. The T-tunnel complex flow fields, however, are representative of pre-tunnel hydrologic conditions. Tunnel excavation promoted drainage of the upper

perched zone of saturation in a region immediately surrounding the tunnel, likely causing a localized depression in water levels. Closure of the tunnel portal in 1992 has resulted in tunnel inundation [13], yet the establishment of water levels to pre-tunnel conditions is not expected to occur until 2020 based on LLNL estimates. The discrepancy between t_0 for the flow and transport simulations is a conservative approach that likely over-estimates the downward potential for radionuclide migration (i.e., heads are increasing from 1992 to 2020 prior to the establishment of pre-tunnel hydrologic conditions), while the $t_0=1992$ for the transport simulations corresponds to a larger radionuclide source mass.

Redistribution of Source Term

A fraction of the radionuclide source term was redistributed from the exchange volumes for each test through the lateral flow of water exiting the tunnel portal and entering the down-slope containment ponds. Tritium mass fractions lost to the containment ponds as computed by LLNL varied significantly between different tests. In particular, MIGHTY OAK and MISSION GHOST experienced containment failures with more than 50% tritium mass loss to the T-tunnel ponds; the other tests had tritium mass losses of less than 20%. The redistribution of radionuclides from each test occurred between t_0 of each test and tunnel closure in 1992. After tunnel closure, the redistribution of radionuclides continued but was limited to the confines of the T-tunnel complex [4,13] with the potential for downward migration through the Tertiary volcanics. The initial particle input illustrated in Fig. 7 is intended to capture the redistribution of radionuclides within the tunnel complex immediately after tunnel closure, $t_0=1992$.

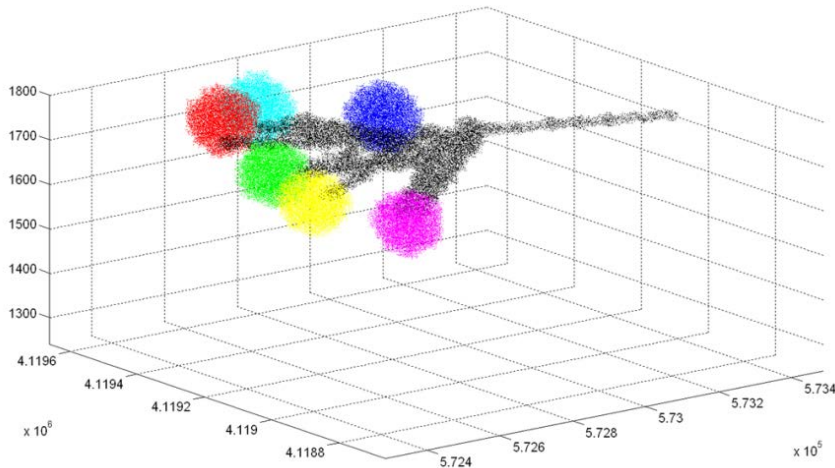


Fig. 7. Radionuclide particle input for the six underground tests (colored spheres) and flooded tunnel waters (black).

Transport Parameters

Cell-by-cell flow terms in the NUFT dual-permeability flow fields are converted by RWHet [4] into matrix and fracture velocities using matrix and fracture continuum porosity values. The dual-domain mass transfer algorithm [7] incorporated into RWHet requires, in addition to fracture and matrix velocities, values of aperture, fracture spacing, effective diffusion, and longitudinal and transverse dispersivities [18]. Aperture and fracture spacing are held constant at 110 microns and 0.18 m for the LCA3 and 100 microns and 0.5 m for the densely welded Tub unit, respectively. Values of fracture spacing and aperture

in the zeolitic tuffs depend on the number of faults and fractures intersecting each grid cell via the fracture continuum method. Random dispersive motion to the radionuclide particle trajectories is incorporated through longitudinal and transverse dispersivities of 0.1 m. Effective diffusion coefficients are the product of the free water diffusion coefficient and the tortuosity factor, τ . Free water diffusion coefficients are assigned to the void area of the T-tunnel complex. A linear isotherm model is used to describe radionuclide adsorption onto the surfaces of the rock matrix and fracture walls. Values of the linear sorption coefficient K_d in Table 1 are used to compute dimensionless retardation coefficients that scale velocity in the matrix and fracture continua.

Treatment of Uncertainty

The uncertainty in source term mass is based on the LLNL analysis of uncertainty in the radionuclide source term inventory provided by [1]. Uncertainty was partitioned by LLNL for tritium, activation products, fission products, and residual fuel and tracer radionuclides (Table 2). Distributions of source mass for each radionuclide in each test are generated by forming minimum and maximum values about the source term masses. These values are used to form either triangular or log-triangular distributions (depending on variability in minimum and maximum values) to randomly assign source term mass independently for each radionuclide in each test.

Table 2. Source mass uncertainty applied to the ten radionuclide source term.

Radionuclides	Uncertainty
3-H	$\pm 300\%$
36-Cl	\pm factor of 10
90-Sr, 99-Tc, 129-I	$\pm 30\%$
238-U, 238-,239-,240-Pu, 241-Am	$\pm 20\%$

The release of radionuclides within the cavity melt glass within the first 100 years is accounted for using LLNL computed minimum and maximum glass dissolution percentages of 0.0052% and 0.67%, respectively. These dissolution percentages are used to form a log-triangular distribution to randomly select a glass dissolution percentage. Randomly selected percentages are then multiplied by the mass of the source term in the glass fraction, and mass released from glass dissolution is applied to the hydraulic release fraction at $t_0=1992$.

The exchange volume distribution of each radionuclide was grouped into two categories as a function of R_c by LLNL: $1.0R_c$ to $1.5R_c$ and $1.5R_c$ to $3.0R_c$ (Table 1). The distribution of radionuclides about the exchange volume is considered uniform, and hence, particles are uniformly distributed within the exchange volumes upon the random selection of size. Exchange volume size is allowed to vary independently for each of the tests in a single transport realization.

Parametric uncertainty in the transport simulations consists of the tortuosity factor, τ , used to compute effective diffusion coefficients and linear sorption coefficient, K_d , used to compute matrix and fracture retardation. A wide range of the tortuosity factor, $0.01 \leq \tau \leq 0.50$, with a central tendency of 0.20 was

derived for rocks on the NNSS [14]. These data are incorporated into the transport model using a log-triangular distribution with a minimum and maximum of 0.01 and 0.50 and mode of 0.20.

Values of the sorption coefficient are allowed to vary according to a lognormal distribution with mean and standard deviation values populated from laboratory values (Table 1). Plutonium represents a special case of radionuclide transport because it exists in both colloidal and aqueous states at the T-tunnel complex. In an effort to represent both states simultaneously, a proposed method by LLNL was implemented that involved decreasing the free water diffusion coefficient by an order of magnitude to represent colloidal-size molecules, and decreasing values of K_d assigned to the fracture walls by two orders of magnitude (Table 1).

Transport Model Results

Radionuclide transport results for the T-tunnel complex tests are based on tracking radionuclide particle trajectories through flow fields with prescribed R7, R11, and R29 flux conditions. Each transport class in Table 1 contains unique transport parameters (i.e., diffusion and sorption coefficients) and exchange volume size. Hence, transport simulations are conducted separately for each of these transport groups. Unprocessed ensemble particle breakthroughs for tritium are first analyzed to investigate transport characteristics of the T-tunnel complex flow fields for the R7, R11, and R29 flux conditions. These breakthroughs are then processed using a complex algorithm that randomly assigns radionuclide mass for each test independently, and then corrects for source mass that exits the tunnel portal to the tunnel ponds, source mass in the redistributed source in the tunnel complex, glass dissolution, and radioactive decay. The flux of particle mass at the water table is then converted to concentration, and these concentrations are screened for regulatory limit exceedance.

Tritium Breakthrough

Tritium particle breakthroughs at the water table are first grouped into yearly bins for the ensemble normalized and cumulative breakthroughs prior to postprocessing of source term mass and radionuclide decay (Fig. 8). These plots reveal several dominant trends for the three flux scenarios. First, cumulative ensemble particle breakthroughs (presented as the fraction of particle breakthrough at the water table to total particles released) are extremely low over the 1,000 year compliance time frame with: $4.2 \times 10^{-3} \%$ (3118 particles), $1.4 \times 10^{-1} \%$ (124,726 particles), and $2.1 \times 10^{-2} \%$ (17,426 particles) for R7, R11 and R29 flux conditions, respectively. These very low breakthroughs indicate that only the very leading edge of the conservative radionuclide source term reaches the water table during the simulation time period. This can also be observed in the irregular breakthrough of the normalized particles despite the very large number of ensemble particles (100,000 per transport realization). Second, particle breakthroughs exhibit a strong threshold response with the applied flux condition. Cumulative breakthroughs range between $4.2 \times 10^{-3} \%$ and $1.4 \times 10^{-1} \%$ for an applied flux range between 11.5 and 15.2 mm/yr. This is a highly non-linear response and a 1 mm/yr increase in applied infiltration between R11 and R29 increases ensemble breakthrough from 17,426 to 124,726 particles (approximately an order of magnitude). Lastly, the lack of breakthrough at early times is consistent with current tritium sampling activities at ER-12-4 that have not detected tritium at the regional water table located in the LCA3.

Further analyses of ensemble tritium particle breakthrough at the water table for R11 (the case with highest applied flux) include particle breakthrough by source and the spatial distribution of particle breakthroughs (Figs. 9 and 10). Analysis of particle breakthroughs by source indicates that the vast majority of these particles originate in either the MISSION GHOST exchange volume (35%) or T-tunnel complex (58%) (Fig. 9). The spatial distribution of breakthroughs for R11 exhibit several dominant trends that further explain the breakthroughs by particle source (Fig. 10). First, breakthroughs are dominated by downward migration along the Mid T-Tunnel fault (denoted as T-Ft-12 on Fig. 3). This large fault intersects the tunnel complex which explains the high degree of tunnel particle breakthrough. Second, the next highest breakthrough is attributed to particles within the MISSION GHOST exchange volume. This exchange volume is intersected by or is very close to fault T-Ft-24 (Fig. 3) and likely facilitates radionuclide particle migration to the water table.

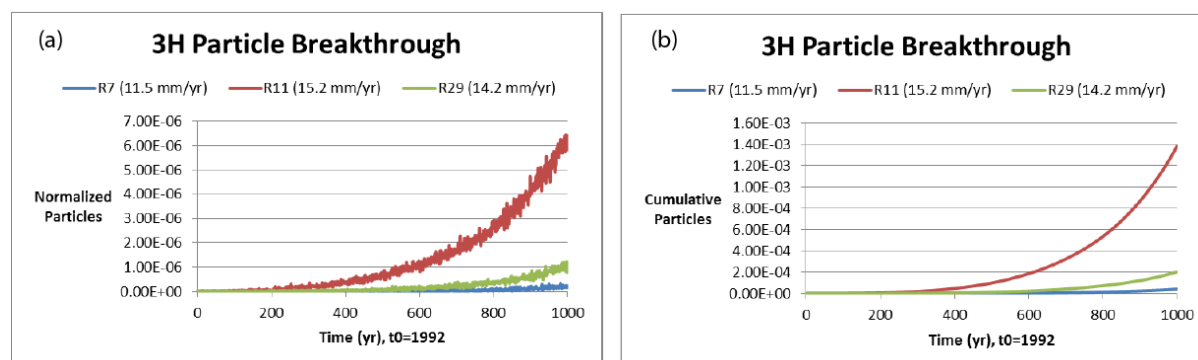
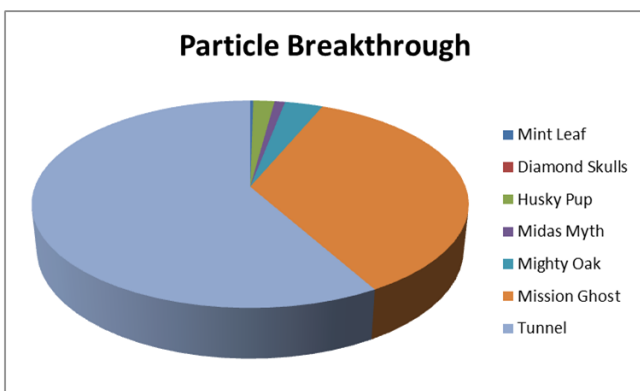


Fig. 8. Normalized (a) and cumulative (b) unprocessed 3-H particle breakthrough for R7, R11, and R29. Note the irregular particle breakthroughs in (a) and extremely low cumulative breakthroughs in (b).



Source	Percent BT
Mint Leaf	0.3
Diamond Skulls	0
Husky Pup	1.8
Midas Myth	0.9
Mighty Oak	3.3
Mission Ghost	35
Tunnel	58

Fig. 9. Particle breakthroughs at the water table as a function of source location.

Third, nearly all of the breakthroughs occur in the synclinal region of the Tertiary volcanics, with little to no breakthrough for tests located above thick portions of the unsaturated carbonates (i.e., DIAMOND SKULLS and MINT LEAF). This is explained by the higher degree of saturation, a greater vertical hydraulic gradient, and sparse degree of fracturing in the Tertiary volcanics as compared to the LCA3. The higher saturation and heads in the Tertiary volcanics result in greater transport velocities along fault structures in the fracture continuum (i.e., fast pathways), whereas the low fracture spacing in the zeolitic

units (12 m average spacing as opposed to 0.18 m average spacing in the LCA3) produces lower rates of diffusion (caused by lower surface area) from higher velocity fractures into the lower velocity matrix. Diffusion is particularly important because dual-domain mass exchange is the dominant retention mechanism for conservative radionuclides.

Fourth, a portion of the particles transmitted to the water table through the Mid T-Tunnel fault originated in the test exchange volumes, and indicates that the tunnel complex (in the numerical model) functions as a macropore that provides connectivity between fault flow paths that would be otherwise isolated. This likely function of the T-tunnel complex was suggested in the conceptual model of fluid flow and radionuclide transport for the site and is strongly supported by these numerical results. Lastly, only 1.4×10^{-1} % of radionuclide particles reached the water table in 1,000 years, and thus, the spatial breakthroughs indicate the fastest pathways only.

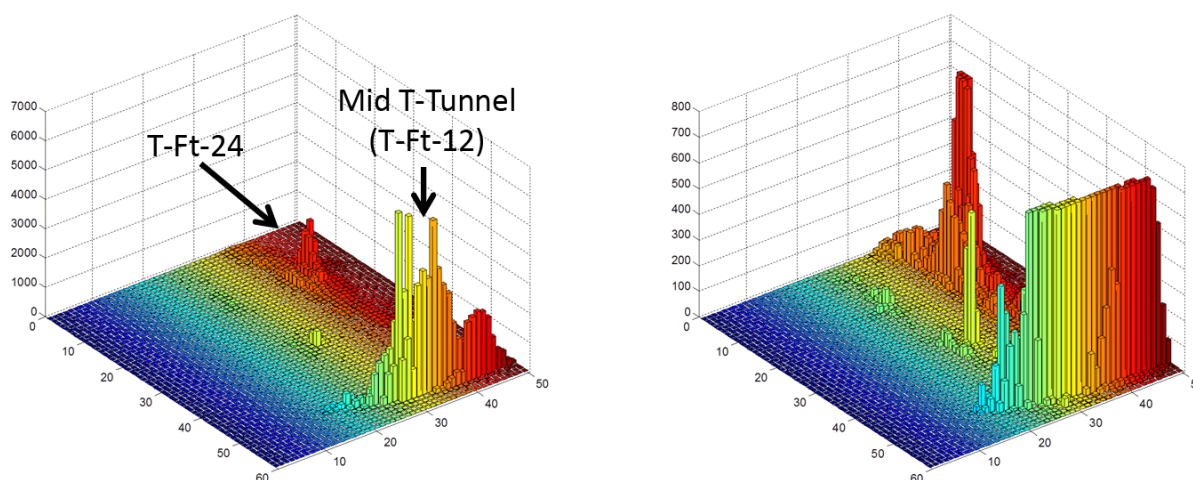


Fig. 10. Particle exit locations for entire tritium transport group ensemble show strong influence of the Mid T-Tunnel fault (T Ft-12 in Fig. 3) on particle breakthrough, with a lesser degree of breakthrough associated with fault T Ft-24. The figure on the right consists of a truncated scale to magnify particle breakthroughs of lower magnitude. Color scale is for illustration purposes only.

Breakthrough of Other Radionuclides

Particle breakthroughs for the other transport classes differ from Transport Class I results because of dissimilar diffusion and sorption coefficients (Table 1). Cumulative particle breakthroughs for the other transport classes for the R11 flux condition are equal to 1.6×10^{-1} % for Transport Classes II and III (36-Cl, 99-Tc, 129-I), a total of 7 particles in the ensemble for Transport Class V (238-U), and 1 particle in the ensemble for Transport Class VI (238-,239-,240-Pu), and no particle ensemble breakthroughs for Transport Classes IV (90-Sr) and VII (240-Am). The slightly higher breakthrough for Transport Class II (1.6×10^{-1} %) than for Transport Class I (1.4×10^{-1} %) reflects the slightly lower diffusion coefficient which decreases the transfer of particles from fractures to low-velocity matrix blocks (Table 1). Particle breakthroughs are rapidly diminished for radionuclides with non-zero K_d values which is to be expected given the very low breakthroughs observed for the conservative radionuclides (i.e., Transport Classes I-

III). Low particle breakthroughs for flow fields with the R11 flux condition, combined with the strong threshold response in breakthrough to applied flux condition, precluded the simulation of the full radionuclide suite through the flow fields with lower flux conditions (i.e., R7, R29).

Processed Radionuclide Breakthroughs

The post-processing of radionuclide particle breakthroughs dramatically changes the shape of the ensemble mass curves depending on particle source mass and radioactive decay. The conversion of ensemble mass to concentration at the water table allows for comparison of radionuclide concentrations to regulatory limits. Post-processing of the Transport Class I particle breakthrough curves shown in Fig. 8 yields tritium concentrations at the water table that do not exceed regulatory limits for either the R7 and R29 flux conditions. Concentrations at the water table for the R11 flux condition are closer to the regulatory limit, with one observed exceedance in year 2017. However, particle breakthroughs are both spatially and temporally irregular and regulatory limit exceedance for tritium occurs from a single particle exiting a cell with lower water table flux. This single exceedance lies outside of the 95-percent confidence intervals and is considered an outlier.

Post-processed breakthroughs generated from flow fields with the R11 flux condition for all other transport classes yield only a single exceedance (239-Pu). This exceedance corresponds to a single particle (out of a total of 9.0×10^7) reaching the water table due to the combination of a high source mass of 239-Pu and a low regulatory limit. The total probability of ^{239}Pu breakthrough according to the simulations is only 1.1×10^{-8} , and similar to tritium, this single particle lies outside of a 95-percent confidence interval. These breakthrough results are based on the highest flux condition (R11) and suggest that regulatory limits at the water table in the LCA3 will not be exceeded for any of the radionuclides for any of the T-tunnel tests.

CONCLUSIONS

Radionuclide transport simulations were conducted for a suite of 10 radionuclides through dual-permeability flow field realizations. The transport simulations incorporated source term and parametric uncertainty in a robust manner involving the execution of 50 transport realizations for each flow field solution, and independently applying source term uncertainty independently to each radionuclide for each of the six tunnel tests. Unprocessed particle trajectories for tritium indicate strong threshold responses with the applied flux condition. All flux conditions produced very low tritium particle breakthroughs with the highest flux condition having a cumulative breakthrough of only 1.4×10^{-1} %. The origin of these particle breakthroughs was predominately the MISSION GHOST exchange volume and flooded waters of the tunnel complex, with water table breakthroughs correlated with faults (i.e., Mid T-Tunnel and T-Ft-21). Post-processed particle breakthroughs, according to a sophisticated post-processing code that represents all relevant processes affecting source term mass, indicate a single occurrence of regulatory limit exceedance for 3-H and 239-Pu. Both of these regulatory limit exceedances represent outliers that are well outside the 95-percent confidence interval.

Uncertainty in the T-tunnel complex transport model consists of radionuclide source term uncertainty and transport parameter uncertainty. Source term uncertainty consists of the initial mass of each radionuclide

for each test at t_0 , melt glass dissolution, and the distribution of each radionuclide over an exchange volume. Transport parameter uncertainty consists of the tortuosity factor used to compute effective diffusion coefficients and sorption coefficients used to compute matrix and fracture retardation. Transport parametric uncertainty and the size of the exchange volume are implemented in the transport model via a transport pre-processor that generates RWHet-specific input files, while uncertainty in source term mass and glass dissolution are incorporated into the final radionuclide transport estimates during post-processing of radionuclide particle breakthroughs.

REFERENCES

1. S. BOWEN, D.L. FINNEGAN, J.L. THOMPSON, et al., "Nevada Test Site radionuclide inventory 1951-1992," Los Alamos National Laboratory, *LA-13859-MS* (2001).
2. J.M. FENELON, "Database of ground-water levels in the vicinity of Rainier Mesa, Nevada Test Site, Nye County, Nevada, 1957-2005," U.S. Geological Survey, *Data Series 190* (2006).
3. E.M. LABOLLE, "RWHet: Random walk particle model for simulating transport in heterogeneous media, Version 3.2 User's Manual and Program Documentation" (2006).
4. LAWRENCE LIVERMORE NATIONAL LABORATORY (LLNL) "Isotopic Analyses: 2006 U12 Tunnel sampling," *Letter report to UGTA sub-Project Director from the LLNL Environmental Radiochemistry Group*, May 5 (2009).
5. D.G. LEVITT and E.M. KWICKLIS, "Infiltration Models for Rainier Mesa and Shoshone Mountain, Nevada, using INFILv3," *Los Alamos National Laboratory LA-UR-12-22984, 2013 Devils Hole Workshop*, Furnace Creek, CA, May 1-3 (2013).
6. J.J. NITAO "User's manual for the US1P module of the NUFT flow and transport code", *Lawrence Livermore National Laboratory* (2004).
7. L. PAN and G.S. BODVARSSON, "Modeling transport in fractured porous media with the random-walk particle method: The transient activity range and the particle transfer probability," *Water Resources Research*, 38, 6 (2002).
8. R. PARASHAR and D.M. REEVES, "Computation of flow and transport in fracture networks on a continuum grid," *Proceedings of MODFLOW and MORE 2011: Integrated Hydrologic Modeling*, Golden, CO, June 5-8, Integrated Groundwater Modeling Center (2011).
9. D.M. REEVES, D.A. BENSON, and M.M. MEERSCHAERT, "Transport of conservative solutes in simulated fracture networks: 1. Synthetic data generation," *Water Resources Research*, 44, W05401 (2008).
10. D.M. REEVES, R. PARASHAR and Y. ZHANG, "Hydrogeologic characterization of fractured rock masses intended for disposal of radioactive waste", In: *Radioactive Waste*, Ed. R.A. Rahman, pp. 351-372, InTech Publishing, Rijeka, Croatia (2012).
11. D.M. REEVES, R. PARASHAR, K. POHLMANN, C. RUSSELL, and J. CHAPMAN, "Development and calibration of dual-permeability models in complex hydrogeologic settings: An example from the T-tunnel complex, Rainier Mesa, Nevada National Security Site," *Proceedings of MODFLOW and MORE 2013: Translating Science into Practice*, Golden, CO, June 2-5, Integrated Groundwater Modeling Center (2013).
12. D.M. REEVES, R. PARASHAR, K. POHLMANN, C. RUSSELL, and J. CHAPMAN, "Development and calibration of dual-permeability flow models with discontinuous fault networks," *Vadose Zone Journal*, in review.

13. C.E. RUSSELL, R.H. FRENCH, R.A. NICHOLSON, et al., "Evaluation of monitoring data from impounded water within U12n and U12t tunnel – Rainier and Aqueduct Mesa, Nevada Test Site," *Desert Research Institute Letter Report* (2003).
14. STOLLER-NAVARRO JOINT VENTURE (SNJV), "Phase II contaminant transport parameters for the ground water flow and contaminant transport model of Corrective Action Unit 98: Frenchman Flat, Nye County, Nevada," *S-N/99205-043* (2005).
15. STOLLER-NAVARRO JOINT VENTURE (SNJV), "Phase I contaminant transport parameters for the groundwater flow and contaminant transport model of Corrective Action Unit 99: Rainier Mesa/Shoshone Mountain, Nevada Test Site, Nye County, Nevada," *S-N/99205-102* (2008).
16. STOLLER-NAVARRO JOINT VENTURE (SNJV), "Phase I hydrologic data for the groundwater flow and contaminant transport model of Corrective Action Unit 99: Rainier Mesa/Shoshone Mountain, Nevada Test Site, Nye County, Nevada," *S-N/99205-103* (2008).
17. W. THORDARSON, "Perched ground water in zeolitized-bedded tuff, Rainier Mesa and vicinity, Nevada Test Site, NV," *U.S. Geological Survey, Report TEI-862* (1965).
18. Y. ZHANG, E.M.LABOLLE, D.M. REEVES, and C. RUSSELL, "Development of RWHet to simulate contaminant transport in fractured porous media", Desert Research Institute Report, DOE/NV/0000939-01 (2012).

ACKNOWLEDGEMENTS

This research was supported by the U.S. Department of Energy, National Nuclear Security Administration Nevada Field Office, UGTA Program. The views and opinions expressed in this paper do not necessarily reflect that of the sponsor. The authors would like to thank Drs. Steve Carle and Yunwei Sun of Lawrence Livermore National Laboratory for productive discussions regarding NUFT simulation.